

Article

# Photophysical and Primary Self-Referencing Thermometric Properties of Europium Hydrogen-Bonded Triazine Frameworks

Chaoqing Yang <sup>1,2,3</sup>, Dimitrije Mara <sup>4</sup> , Joydeb Goura <sup>5</sup> , Flavia Artizzu <sup>6,\*</sup>  and Rik Van Deun <sup>3</sup> 

<sup>1</sup> Department of Chemistry, Zhejiang University, Hangzhou 310027, China

<sup>2</sup> ZJU-Hangzhou Global Scientific and Technological Innovation Center, Hangzhou 311215, China

<sup>3</sup> L3—Luminescent Lanthanide Lab, Department of Chemistry, Ghent University, Krijgslaan 281-S3, 9000 Ghent, Belgium

<sup>4</sup> Institute of General and Physical Chemistry, Studentski trg 12/V, 11000 Belgrade, Serbia

<sup>5</sup> Engineering Science & Technology Division, CSIR-North-East Institute of Science & Technology, Jorhat 785006, Assam, India

<sup>6</sup> Department of Sustainable Development and Ecological Transition (DISSTE), University of Eastern Piedmont “A. Avogadro”, Piazza S. Eusebio 5, 13100 Vercelli, Italy

\* Correspondence: flavia.artizzu@uniupo.it

**Abstract:** Lanthanide hydrogen-bonded organic frameworks (LnHOFs) are recently emerging as a novel versatile class of multicomponent luminescent materials with promising potential applications in optics and photonics. Trivalent europium ( $\text{Eu}^{3+}$ ) incorporated polymeric hydrogen-bonded triazine frameworks (PHTF:Eu) have been successfully obtained via a facile and low-cost thermal pyrolysis route. The PHTF:Eu material shows a porous frame structure principally composed of isocyanuric acid and ammelide as a minor constituent. Intense red luminescence with high colour-purity from  $\text{Eu}^{3+}$  is obtained by exciting over a broad absorption band peaked at 300 nm either at room or low temperature. The triazine-based host works as excellent optical antenna towards  $\text{Eu}^{3+}$ , yielding ~42% sensitization efficiency ( $\eta_{\text{sens}}$ ) and an intrinsic quantum yield of  $\text{Eu}^{3+}$  emission ( $\Phi_{\text{Eu}}$ ) as high as ~46%. Temperature-dependent emission studies show that PHTF:Eu displays relatively high optical stability at elevated temperatures in comparison to traditional inorganic phosphors. The retrieved activation energy of 89 meV indicates that thermal quenching mechanisms are attributed to the intrinsic energy level structure of the metal-triazine assembly, possibly via a thermally activated back transfer to ligand triplet or CT states. Finally, by using an innovative approach based on excitation spectra, we demonstrate that PHTF:Eu can work as a universal primary self-referencing thermometer based on a single-emitting center with excellent relative sensitivity in the cryogenic temperature range.

**Keywords:** luminescence; lanthanides; hydrogen bonding; HOFs; thermometry



**Citation:** Yang, C.; Mara, D.; Goura, J.; Artizzu, F.; Van Deun, R.

Photophysical and Primary Self-Referencing Thermometric Properties of Europium Hydrogen-Bonded Triazine Frameworks.

*Molecules* **2022**, *27*, 6687. <https://doi.org/10.3390/molecules27196687>

Academic Editor: Alistair J. Lees

Received: 8 September 2022

Accepted: 24 September 2022

Published: 8 October 2022

**Publisher's Note:** MDPI stays neutral with regard to jurisdictional claims in published maps and institutional affiliations.



**Copyright:** © 2022 by the authors. Licensee MDPI, Basel, Switzerland. This article is an open access article distributed under the terms and conditions of the Creative Commons Attribution (CC BY) license (<https://creativecommons.org/licenses/by/4.0/>).

## 1. Introduction

Hydrogen-bonded nanomaterials are attractive hosts for a wide range of biological guests, such as biomacromolecules and biocatalysis agents. Recently, the emerging class of hydrogen bonded organic frameworks (HOFs) based on the molecular self-assembly via non-covalent interactions, mainly hydrogen bonding, of organic building blocks, have demonstrated a set of properties that makes them promising for biological fluorescence labelling, sensing, anti-counterfeiting, and illumination. The constitutional units of HOFs are usually highly rigid molecules featuring aromatic moieties with a large  $\pi$ -conjugated system, which are typically suitable to yield interesting luminescent properties [1]. Depending on the degree of  $\pi$ -conjugation, organic compounds can capture and emit photons in tunable wavelength ranges, which facilitates the rational design of luminescent HOF materials with versatile colors. Moreover, the structure of these frameworks widely involves a variety of intermolecular interactions including electrostatic,  $\pi$ - $\pi$  stacking, and van der Waals forces, enabling charge transfer transitions between the constituting  $\pi$ -conjugated

systems which could significantly affect and enhance the emission [1–5]. For example, the hydrogen-bond-mediated supramolecular interactions between different chain moieties in polymer carbon dots allow for electronic transitions between spatially separated molecular orbitals leading to emission enhancement [5].

However, despite the high versatility of luminescent HOFs, their emission properties are characterized by low “color-purity” (broad emission bands), relatively small Stokes’ shifts, and typical nanosecond-ranged lifetimes, limiting their potential biosensing/biolabelling and temperature sensing applications. Trivalent lanthanide cations ( $\text{Ln}^{3+}$ ), on the other hand, have very narrow absorption and emission lines, showing large apparent Stokes’ shifts, long emission decay times and excellent response to temperature changes [6]. These features have made lanthanide luminescence of great importance in a variety of applications, encompassing not only hi-tech photonic devices, but also potential biological immunoassays and non-contact temperature probes [6–8]. However,  $\text{Ln}^{3+}$  ions’ luminescence is a result of transitions within the partially filled 4f shells. As these transitions are parity-forbidden, this leads to low molar absorption coefficients resulting in inefficient optical excitation and weak emission [9]. Our previous researches have shown that HOFs can be conveniently used as a tunable platform for constructing multi-emissive lanthanide (Ln) molecular materials [10–13]. Despite the interest in these materials, there are still few reports about the description of the fundamental photophysical properties of lanthanide ions in doped HOFs and limited understanding has been achieved on the structure/properties relationship of these materials. Moreover, the ratiometric temperature sensing properties of lanthanide-doped HOFs have been very scarcely investigated and mostly based on the dual emission from the matrix and  $\text{Eu}^{3+}$  in a restricted temperature range [14]. However, the poor intrinsic structural/morphological definition, the high flexibility, and the extreme sensitivity to external stimuli, such as moisture or various chemical species, of such doped polymeric materials, could easily lead to instability of the temperature sensing performances which would require constant accurate calibration.

Here, we report a  $\text{Eu}^{3+}$ -incorporated polymeric hydrogen-bonded triazine framework (PHTF:Eu) synthesized by a facile solid phase thermal pyrolysis route and provide an insight on the factors that govern its emission efficiency via photoluminescence (PL) steady state and time-resolved measurements as well as absolute quantum yields and temperature-dependent PL studies. Moreover, we investigate the potential application of this material as a ratiometric primary and self-referencing thermometer in the 10–410 K temperature range based on a universal approach that relies on the photoluminescence excitation (PLE) spectra instead of the PL-based conventional method. This approach, which solely takes into account  $\text{Eu}^{3+}$ -centered lines, is particularly suitable for this class of doped HOFs materials as it allows for applying single-center-based ratiometric temperature sensing while bypassing the often uncontrolled ligand-to-metal, metal-to-metal, and spurious external energy transfer as well as possible inhomogeneous ligand/crystal field effects, yielding an univocally defined thermometric equation.

## 2. Results and Discussion

### 2.1. Structure and Morphology of PHTF:Eu

The PHTF material and its  $\text{Eu}^{3+}$ -doped derivatives PHTF:Eu of different  $\text{Eu}^{3+}$  concentrations were synthesized at 255 °C via a solid phase thermal pyrocondensation reaction from a precursor obtained from a wet reaction between  $\text{Eu}^{3+}$  and urea (U) labelled as U-Eu (the detailed description is given in the Experimental Section). In order to identify the structure of the as-synthesized material, PXRD measurements were carried out at room temperature. The PXRD pattern of the pristine PHTF matrix shown in Figure 1a is consistent with the characteristic peaks of isocyanuric acid. Two well-resolved peaks at lower angles, 19.8° and 22.3°, are attributed to the in-planar packing between isocyanuric acid molecules through multiple N–H···O H-bonds [15]. Another strong broad peak at 29.7°, corresponding to a *d*-spacing of 0.32 nm supports the  $\pi$ - $\pi$  stacking of individual isocyanuric acid nanolayers as shown in Figure 1b [16]. All PHTF:Eu samples exhibit

similar reflection peaks as the pristine PHTF. With the increase in  $\text{Eu}^{3+}$  doping, a diffraction peak at  $29.7^\circ$ , significantly decreases in intensity, which might be due to the  $\text{Eu}^{3+}$  ions affecting the in-plane packing of H-bonded molecules [10]. The enlarged PXRD pattern shown in Figure S1 reveals that the obtained PHTF contains a minor amount of ammelide. No characteristic peaks of  $\text{Eu}_2\text{O}_3$  and  $\text{Eu}(\text{NO}_3)_3 \cdot x\text{H}_2\text{O}$  were found in PHTF-4Eu.

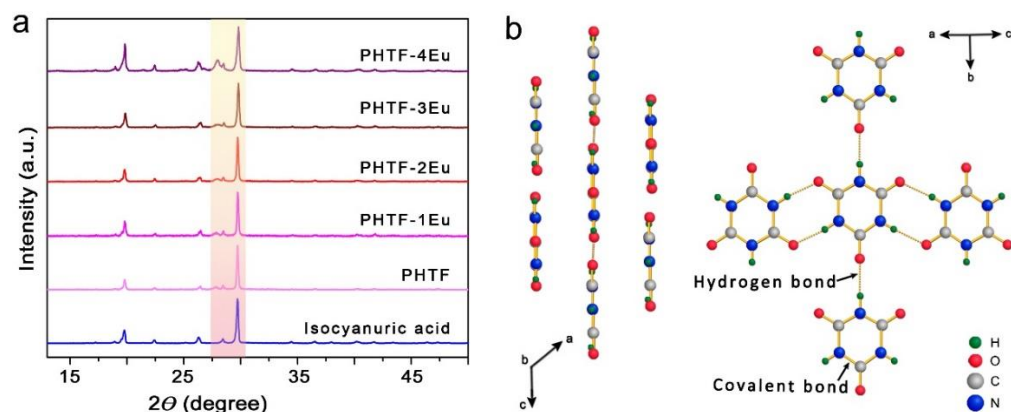


**Figure 1.** (a) Normalized PXRD patterns of PHTF, PHTF:Eu, and pure isocyanuric acid; (b) Scheme showing how an isocyanuric acid monomer connects to other neighboring in-plane or out-of-plane units through eight  $\text{N}-\text{H}\cdots\text{O}$  H-bonds. Covalent bonds are shown as saffron yellow solid lines and H-bonds as yellow dotted lines.

The CHN elemental analysis, shown in Table S1, confirmed the observations made from the PXRD results. The PHTF has a composition in close proximity with the theoretical wt % of cyanuric acid. The slightly high nitrogen content in PHTF should originate from the ammelide impurity. Upon increasing the  $\text{Eu}^{3+}$  loading, the carbon, hydrogen, and nitrogen content of the PHTF:Eu gradually decreased, which might be due to the increase in structure defects in the PHTF framework [10]. The N/C ratio slightly increases due to the polycondensation of isocyanuric acid into ammelide at temperatures exceeding  $250^\circ\text{C}$  [17]. The actual  $\text{Eu}^{3+}$  concentration in PHTF:Eu was investigated by ICP-MS analysis and the results show that the maximum content achieved in PHTF-4Eu is below 9% wt (Table S2). The morphologies of the PHTF and PHTF:Eu samples were investigated by SEM and TEM microscopy. The pristine PHTF as well as the PHTF:Eu samples have a similar but quite irregular morphology consisting of small flakes and large agglomerates with particle sizes between 0.3 and  $5\ \mu\text{m}$  (Figures S2 and S3). The TEM images show that PHTF (Figure S2) as well as PHTF-2Eu (Figure 2a,b) present an irregular hollow structure with different cavity volumes. The blocky structure is slightly cracked after  $\text{Eu}^{3+}$  ions doping. The STEM-EDX mapping confirmed the homogeneous distribution of  $\text{Eu}^{3+}$  in the PHTF structures (Figure S2e–h).

FT-Raman spectroscopy has been used to investigate the molecular and lattice vibrations of PHTF. As shown in Figure S4a, the spectrum of pristine PHTF is in good agreement with the characteristic peaks of the solid isocyanuric acid which displays a series of peaks located at 525, 552, 703, 991, and  $1725\ \text{cm}^{-1}$ . The most intense peak at  $703\ \text{cm}^{-1}$  is related to the ring out-of-plane bending vibration. Another peak at  $1725\ \text{cm}^{-1}$  could be ascribed to the  $\text{C}=\text{O}$  stretching vibration [11]. The normalized FT-Raman spectra of pristine PHTF and  $\text{Eu}^{3+}$ -doped PHTF are given in Figure 2c. The peak at  $1725\ \text{cm}^{-1}$  originating from the  $\text{C}=\text{O}$  stretching vibration steadily weakens upon increasing the  $\text{Eu}^{3+}$  concentration, which suggests that the  $\text{C}=\text{O}$  group effectively coordinates europium ions. The enlarged FT-Raman curves shown in Figure S4b reveals that a peak at  $1015\ \text{cm}^{-1}$  attributed to the ring breathing vibration of ammelide molecules becomes more pronounced, which is in accordance with the XRD results. No evidences of residual urea,  $\text{Eu}(\text{NO}_3)_3$ , or  $\text{Eu}_2\text{O}_3$  nanoparticles are found for PHTF:Eu, as shown in Figure S4c. Similar information can be drawn from the DRIFTS spectra shown in Figure 2d. The stretching vibration of the

carbonyl group at  $1500\text{ cm}^{-1}$  and the ring vibration bands at  $770$  and  $1200\text{ cm}^{-1}$  were found to become progressively weaker for the PHTF:Eu samples [15,18]. These results further hint at a dentate bridging coordination mode for the PHTF units through C=O groups coordinating  $\text{Eu}^{3+}$  ions [13].

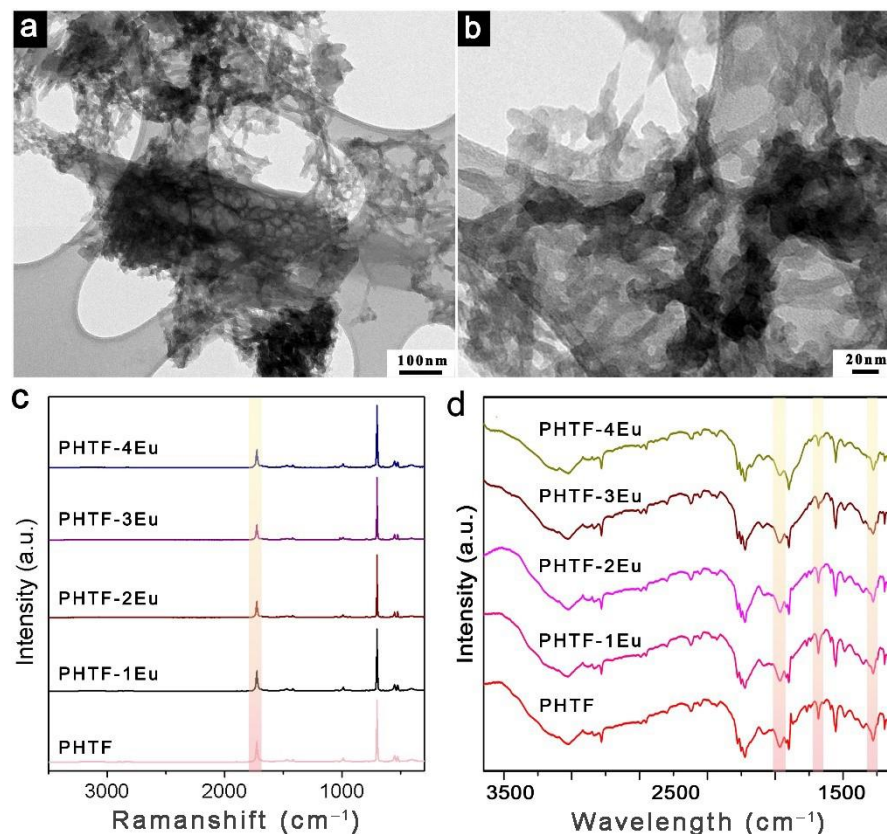


**Figure 2.** (a,b) TEM images of PHTF-2Eu at different magnifications; (c) Normalized FT-Raman spectra of PHTF and PHTF:Eu; (d) Normalized DRIFTS spectra of PHTF and PHTF:Eu.

In order to get more insight into the pyrolysis mechanism of PHTF:Eu, thermogravimetric (TG) analysis was carried out under air. It is known that, upon heating, urea undergoes condensation reactions with elimination of ammonia [17]. The TG curve of pure urea (Figure 3a) exhibits mass losses in three stages. The first major mass loss of about 50.3% can be attributed to the rapid deamination of urea forming isocyanuric acid and a small quantity of ammelide. The second stage corresponds to a thermal condensation process where those compounds are transformed into polymeric carbon nitride [17]. A third step begins after  $400\text{ }^{\circ}\text{C}$ , where all materials gradually sublime, and the organic components eventually decompose completely. Accordingly, the derivative thermo-gravimetric analysis (DTG) curve of urea shows three distinct DTG peaks,  $225\text{ }^{\circ}\text{C}$ ,  $376\text{ }^{\circ}\text{C}$ , and  $519\text{ }^{\circ}\text{C}$  (Figure 3b). The europium trinitrate prominently influences the pyrolysis of urea. Compared to the pyrolysis of pristine urea, the  $\text{Eu}^{3+}$  doped urea presents more rapid mass losses, which indicates that the incorporated  $\text{Eu}^{3+}$  ions accelerate the polycondensation process [19].

## 2.2. Emission Colour Purity of PHTF:Eu

An extensive investigation of the photoluminescence (PL) properties of the as-synthesized samples was conducted. The PL properties of  $\text{Eu}^{3+}$  doped samples were investigated both before (U-3Eu) and after (PHTF-3Eu) heat treatment. In the excitation spectrum of U-3Eu monitored at  $612\text{ nm}$ , the most intense emission peak of  $\text{Eu}^{3+}$ , a weak broad band can be seen between  $250$  and  $310\text{ nm}$ , as well as a series of sharp peaks extending from  $300$  to  $500\text{ nm}$  (Figure 4a). These sharp peaks can be reliably attributed to inner 4f shell transitions of  $\text{Eu}^{3+}$ . All labelled peaks have been assigned to appropriate transitions in Table S3. The broad

excitation band for U-3Eu can be ascribed to a Eu-O charge-transfer transition (Figure S5a) or ligand-to-metal transitions giving rise to energy transfer from the urea matrix to  $\text{Eu}^{3+}$  dopants. For PHTF-3Eu, the broad excitation band of higher intensity at longer wavelengths (308 nm) might be attributed to ligand-to-metal transitions (Figure S5b), which indicates a more effective interaction between  $\text{Eu}^{3+}$  ions and the PHTF matrix [20].

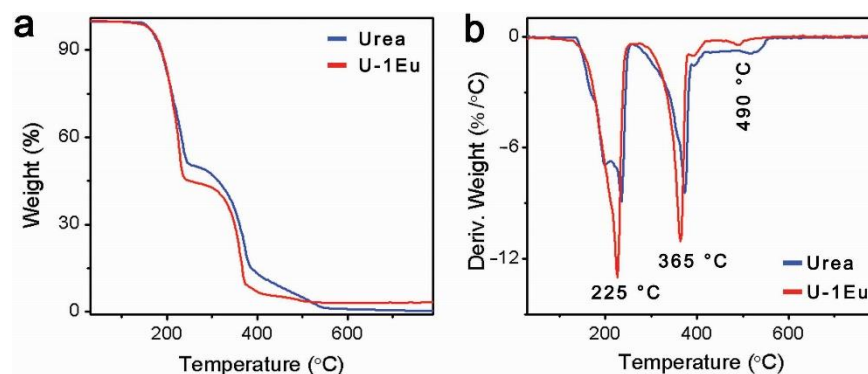


Figure 3. (a) TG and (b) DTG curves of urea and U-1Eu.

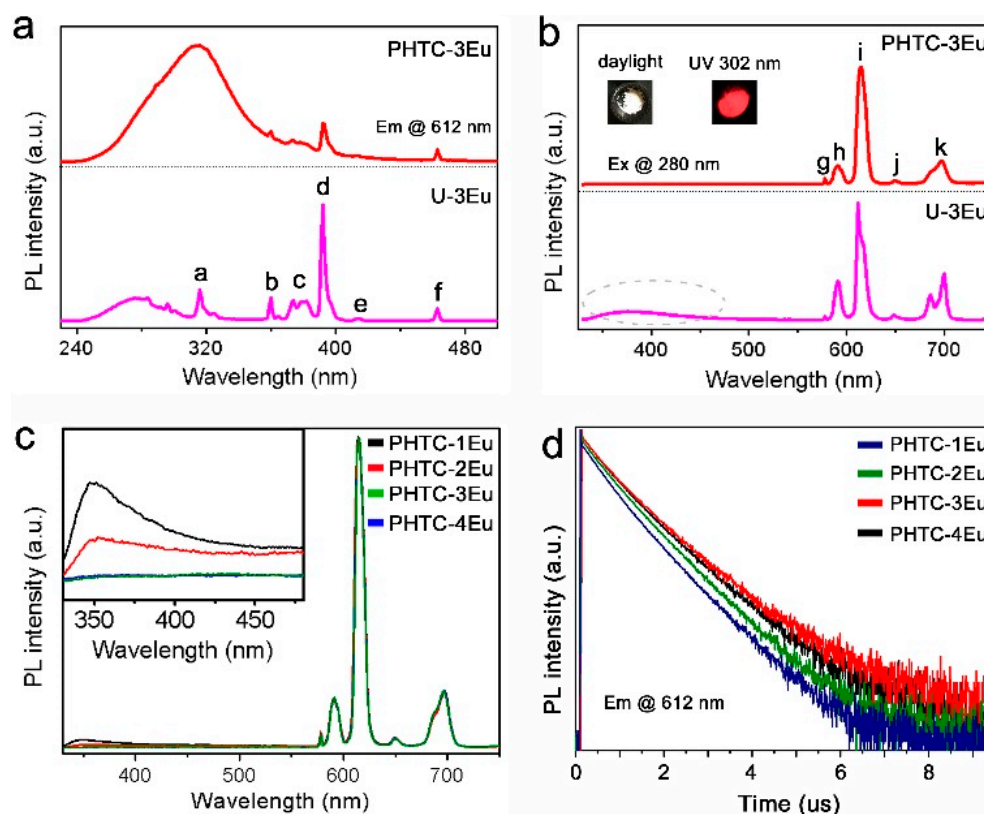


Figure 4. (a) Normalized excitation ( $\lambda_{em} = 612$  nm) and (b) emission spectra ( $\lambda_{ex} = 280$  nm) of PHTF-3Eu and U-3Eu. Insert: photos of PHTF-3Eu under daylight and a 302 nm UV lamp. (c) Normalized emission spectra of PHTF:Eu excited at 280 nm, Insert: enlarged emission spectra of PHTF:Eu samples in the range of 330 to 480 nm. (d) PL decay curves of PHTF:Eu excited at 280 nm.

The emission spectra (Figure 4b) of the two samples are observed after exciting into the broad absorption band at 280 nm. It could be clearly seen that both samples yield strong sharp peaks attributed to the characteristic  $\text{Eu}^{3+}$  f-f transitions. The emission spectrum of U-3Eu presents a broad band in the region of 330–480 nm, which indicates that the energy transfer from urea to  $\text{Eu}^{3+}$  is not fully efficient. On the other hand, after heat treatment, only the strong f-f transition peaks of  $\text{Eu}^{3+}$  are observed for PHTF-3Eu.

As shown in Figure 4b, PHTF-3Eu shows bright red luminescence with CIE (CIE, 1931) coordinates of (0.657, 0.337) approaching the Rec. 2020 (0.708, 0.292) [21] Red Primary light specification. The normalized emission spectra for PHTF:Eu with different  $\text{Eu}^{3+}$  concentrations show similar profiles (Figure 4c). However, the matrix emission bands in the 330–480 nm region change and constantly weaken upon increasing  $\text{Eu}^{3+}$  concentration as a result of the increased number of acceptors. The calculated CIE chromaticity coordinates of PHTF:Eu (Table S4) also clearly show that the concentration of  $\text{Eu}^{3+}$  ions influences the colour-purity (Figure S5c). The decay dynamics (Figure 4d) of  $\text{Eu}^{3+}$  in all samples follows a monoexponential trend with retrieved time constants of 523.6, 534.9, 549.2, and 540.9  $\mu\text{s}$  for PHTF-1Eu, PHTF-2Eu, PHTF-3Eu, and PHTF-4Eu, respectively (Table S5). The slight decrease in the decay time constant for PHTF-4Eu might be attributed to a concentration quenching effect of  $\text{Eu}^{3+}$  ions.

The following discussion on the  $\text{Eu}^{3+}$  sensitization mechanism and the thermal response of the emission will be focused on PHTF-3Eu as this sample showed the highest emission intensity.

### 2.3. $\text{Eu}^{3+}$ Sensitization in PHTF:Eu

The sensitization efficiency ( $\eta_{\text{sens}}$ ) from the donor PHTF matrix to  $\text{Eu}^{3+}$  could be calculated and analysed according to the following Equation (1) [22]:

$$\eta_{\text{sens}} = \frac{\Phi}{\Phi_{\text{Eu}}} \quad (1)$$

where  $\Phi$  is the overall quantum yield which can be readily measured through the use of an integration sphere, and the intrinsic quantum yield of Eu ions ( $\Phi_{\text{Eu}}$ ) which can be deduced by Equations (S1) and (S2). These equations however require the determination of the electric and magnetic transition dipole strengths which are quite difficult to retrieve. However, since the characteristic  $\text{Eu}^{3+}$  transition,  $^5\text{D}_0 \rightarrow ^7\text{F}_1$  is only magnetic dipolar in nature, its intensity does not depend on the crystal field. Fortunately, this offers a way to greatly reduce the experimental parameters needed and  $\Phi_{\text{Eu}}$  could be calculated from the corrected emission spectrum and time-resolved photoluminescence data via a simplified Einstein's equation for spontaneous emission (Equation (2)) [22]:

$$\Phi_{\text{Eu}} = \frac{\tau_{\text{obs}}}{\tau_{\text{rad}}} = \frac{\tau_{\text{obs}} A_{\text{MD}} n^3 I_{\text{TOT}}}{I_{\text{MD}}} \quad (2)$$

where  $\tau_{\text{obs}}$  is the actual lifetime of the emitting excited state, and  $\tau_{\text{rad}}$  is the radiative lifetime of this state in absence of any non-radiative de-activation processes.  $A_{\text{MD}}$  is the spontaneous radiative rate for the  $\text{Eu}^{3+} ^5\text{D}_0 \rightarrow ^7\text{F}_1$  magnetic dipole transition and is taken as  $14.65 \text{ s}^{-1}$  [22].  $n$  is the refractive index of the medium whose value was taken as 1.748 for cyanuric acid.  $I_{\text{TOT}}/I_{\text{MD}}$  is the ratio of the total integrated area of the  $\text{Eu}^{3+}$  emission spectrum to the area of the  $^5\text{D}_0 \rightarrow ^7\text{F}_1$  band. Table 1 presents the main photophysical parameters for the investigated samples. As it can be seen, the change in the crystal/ligand field upon thermal treatment and transformation of the organic matrix has a relevant influence on the oscillator strength of  $\text{Eu}^{3+}$  emission leading to a dramatic decrease in the radiative lifetime.

**Table 1.** Main photophysical parameters of U-3Eu and PHTF-3Eu.

Parameter	U-3Eu	PHTF-3Eu
$\tau_{\text{RAD}}$	1.943 ms	1.196 ms
$\tau_{\text{OBS}}$	0.399 ms	0.549 ms
$I_{\text{TOT}}/I_{\text{MD}}$	6.6	10.7
$\Phi$	5.5%	19.2%
$\Phi_{\text{Eu}}$	20.6%	45.9%
$\eta_{\text{sens}}$	26.7%	41.8%

The absolute overall quantum yield for PHTF-3Eu, directly measured with an integrating sphere, was found to be 19.2% (Figure S6), much higher than in U-3Eu (5.5%). These values are in agreement with the retrieved lifetimes of  $\text{Eu}^{3+}$  emission at 612 nm, which were found to be 399.2  $\mu\text{s}$  (Table S6) for U-3Eu (Figure S7) and 549.2  $\mu\text{s}$  for PHTF-3Eu. A reliable interpretation for this result is that  $\text{Eu}^{3+}$  emission in the hydrated urea matrix is strongly influenced by the presence of quenching sites, such as  $-\text{OH}$  and  $-\text{NH}$  groups [23,24]. However, the thermal treatment at 265 °C leads to a series of pyrolysis reactions of urea to form isocyanuric acid, yielding a dehydrated PHTF:Eu material. As a result, the PHTF-3Eu sample displays an improved  $\text{Eu}^{3+}$  intrinsic quantum yield (45.9%) with respect to its urea-based precursor (20.6%). Importantly, a high sensitization efficiency of 41.8% is found for the PHTF-Eu system. This value, although not comparable to the best results obtained in small molecular complexes where all the antenna units are directly coordinated to the lanthanide acceptor [25,26], is significantly higher than in most Eu-doped systems, such as Eu-doped silica nanoparticles (38%) and Eu-doped  $\text{YPO}_4$  nanocrystals capped with an organic antenna (26%) [27,28]. The reason for this enhanced ligand-to-metal energy transfer efficiency mainly relies on two factors. The first is of spectral origin and is related to the high-lying excited ligand donor energy levels, (above 28,000  $\text{cm}^{-1}$ ) associated to a very broad emission (Figure S5b) which ensure an excellent spectral overlap with the  $\text{Eu}^{3+}$  acceptor absorption through the upper energy levels manifold ( $^5\text{D}_3$  to  $^5\text{D}_0$  at  $\sim 24,400$ – $17,200$   $\text{cm}^{-1}$ ) (Figure S8a). The second factor is instead related to the overall kinetics of the process. As previously observed in analogous Eu-doped HOFs semiconducting materials [10], the excited state depopulation of the organic moiety can follow different pathways: (i) intramolecular radiative or nonradiative deactivation; (ii) energy transfer to directly coordinated  $\text{Eu}^{3+}$  ions; and (iii) charge transfer or exciton migration over the network. This latter phenomenon is significantly enhanced by the establishment of H-bonds within the PHTF matrix (Figure 1b) which increases the rigidity of the network and facilitates interring interactions, including  $\pi$ -stacking. The enhanced exciton migration throughout the H-bonded network increases the chances of energy transfer to  $\text{Eu}^{3+}$  centers working as “localized traps” in doped materials where the donor-acceptor ratio is significantly above unity ( $>10$  in our case), hence leading to improved sensitization efficiency. In addition, the increased rigidity of the system favors intersystem crossing from singlet-to-triplet excited states and suppresses the non-radiative decay channels [23] thus favoring ligand-to-metal energy transfer, which is believed to occur through the excited ligand triplets (Figure S8a).

#### 2.4. Temperature-Dependent Emission of PHTF:Eu

The thermal response of the PL properties in Ln doped materials is one of the most important parameters for potential applications, and is also fundamental to disclose the structure of energy levels in the material. As shown in Figure 5a, the PL intensity of PHTF-3Eu, taken as a representative example, monotonically decreases with increasing temperature in the range from 10 K to 410 K. No peak shift of  $\text{Eu}^{3+}$  emission or changes in the full widths at half-maximum (FWHM) are observed. The emissive band related to the PHTF matrix also shows an absolute decrease in intensity, but it gradually enhances with respect to the normalized  $\text{Eu}^{3+}$  emission (Figure S9) upon increasing the temperature. However, as evidenced in Figure 4b and discussed in the above paragraph, the weak absolute intensity of PHTF-related emission, originated from the efficient sensitization of  $\text{Eu}^{3+}$ , allows PHTF-3Eu to keep a stable emission color purity (Figure 5c) over a broad range of temperatures with relevant deviations of the CIE chromaticity coordinates (Table S7) only at 410 K. The observed thermal stability of the emission color is a beneficial feature for applications in electrically driven optical devices such as LEDs. On the other hand, this behavior does not consent the use of the PL response for a reliable ratiometric temperature sensing based on dual emission [14]. The thermometric properties of PHTF:Eu will be discussed further; nonetheless, important considerations about the thermal quenching mechanism of  $\text{Eu}^{3+}$  emission can be made here.

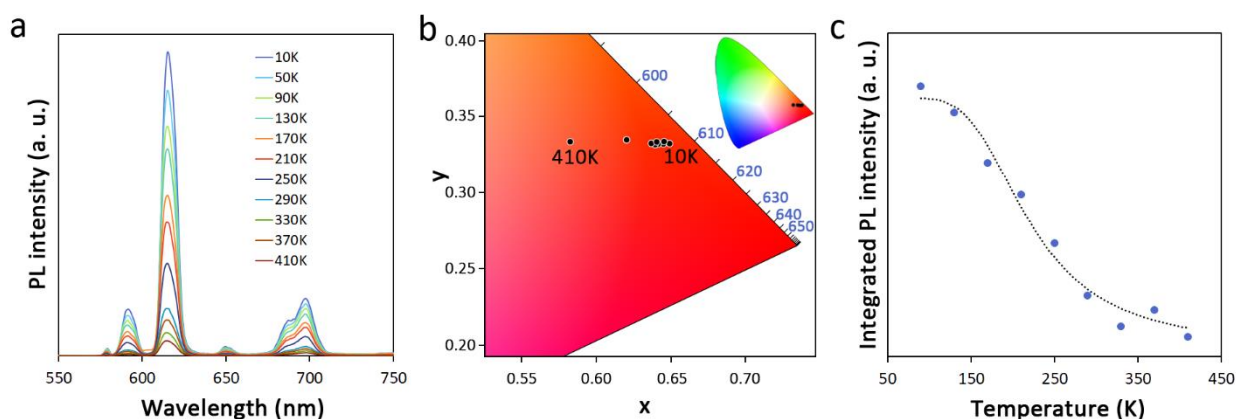


**Figure 5.** (a) Temperature-dependent PL spectra of PHTF-3Eu ( $\lambda_{\text{ex}} = 300$  nm); (b) Magnification of a portion of the CIE diagram of PHTF:Eu in the 10–410 K temperature range. The whole diagram is reported in the inset; (c) Plot of the integrated PL intensity vs. temperature for the emission band centered at 612 nm ( $I_{02}$ ,  ${}^5\text{D}_0 \rightarrow {}^7\text{F}_2$ ) of PHTF-3Eu. The blue circles represent the experimental data, and the dotted curve represents the best fit according to Equation (4) ( $R^2 = 0.975$ ).

The experimental integrated intensity  $I$  of  $\text{Eu}^{3+}$  emission from the  ${}^5\text{D}_0$  excited state as a function of the absolute temperature is reported in Figures 5b and S9a. As the temperature increases, some nonradiative channels become thermally activated and this results in a decrease in the luminescence intensity. We fitted the data with a classical Mott-Seitz model [29,30], according to the following Equation (3):

$$I(T) = \frac{I_0}{1 + A \exp\left(-\frac{E_a}{k_B T}\right)} \quad (3)$$

where  $I_0$  is the peak intensity at temperature  $T = 0$  K,  $A$  is a parameter related to the radiative lifetime ( $\tau_{\text{rad}}$ ) as  $A = \tau_{\text{rad}}/\tau_0$ ,  $E_a$  is the activation energy in the thermal quenching process, and  $k_B$  is the Boltzmann constant. The best fitting results were retrieved for the 90–410 K temperature range and the resulting curve is reported as a dotted line in Figure 5b. The inclusion of low temperature (10–50 K) data brings significant deviations and lowers the quality of the fit, whereas a consistent improvement is found when fitting with an extended double-term Mott-Seitz model (Equation (S4)) [6], which takes into account the competition of multiple excited-state deactivating channels (Figure S10 and Table S8). However, this model yields results of difficult interpretation and one activation energy value (10 meV) that is physically unreasonable; therefore, in the following discussion, we rely on the fitting results of the classical Mott-Seitz model in the restricted temperature range, as reported in Figure 5c. The retrieved activation energy of PHTF-3Eu of 89 meV ( $719 \text{ cm}^{-1}$ ) is significantly higher than what was found in undoped polymeric  $g\text{-C}_3\text{N}_4$  materials [31] as well as in many other luminescent semiconducting nanostructures such as ZnO, CdTe, and carbon nanoparticles [32–34], indicating a relatively high stability of the luminescence properties on temperature changes (Table 2). In regard to the origin of the thermal quenching, we first note that the relatively low  $E_a$  value found is not compatible with a deactivation pathway through multiphonon relaxation related to high energy vibrational modes of OH groups ( $\sim 3400 \text{ cm}^{-1}$ ) [24]. This observation is also in agreement with the relatively strong dependence of the emission intensity on the temperature, even below 200 K, where high-energy vibrational quanta of organic groups are hardly populated. Likewise, quenching by material defects does not seem plausible in this case given the monoexponential decay dynamics of  $\text{Eu}^{3+}$  emission from the  ${}^5\text{D}_0$  level (Figure 4d), which typically indicates matrix homogeneity. This leaves the source of thermal quenching to the internal energy level structure of the organic moiety- $\text{Eu}^{3+}$  metal ion assembly. Nonetheless, the activation energy found for PHTF-3Eu is much lower than that retrieved for  $\text{Eu}(\text{thd})_3$  (thd = 2,2,6,6-tetramethyl-3,5-heptanedionato)

complex in the gas phase (510.8 meV), where the shortening of the  $\text{Eu}^{3+} {}^5\text{D}_0$  lifetime on temperature increase was attributed to the deactivation through a low-lying ligand-to-lanthanide charge transfer (CT) state [35,36]. Our results are, however, fully in agreement with those recently reported for a  $\text{Eu}^{3+}$  ketoprofen adduct, whose PL data were best fitted with the extended Mott-Seitz model yielding  $E_{a1} = 61$  meV ( $494 \text{ cm}^{-1}$ ) and  $E_{a2} = 0.5$  meV ( $3.8 \text{ cm}^{-1}$ ) [37]. Despite the triplet excited state level for the triazine moiety lying well above  $22,000 \text{ cm}^{-1}$  [38], the wide triplet band broadening typically observed in organic antenna sensitized lanthanide compounds [39] can justify thermally activated energy back transfer to the triplet state or to a low-lying CT state involving the organic triazine units (Figure S8) [36], or possibly a competition between these two deactivation channels. A more in-depth interpretation of the temperature-dependent emission quenching will require more extended dedicated studies that will be the subject of future work.

**Table 2.** Activation energies of various emitting materials.

Material	$E_a$ (meV)	Reference
CdTe	47	[33]
ZnO	59	[34]
carbon nanoparticles	42.7	[32]
Polymeric carbon nitride	73.6	[31]
PHTF:Eu	89	This work
$\text{Eu}(\text{thd})_3$ (in gas phase)	510.8	[36]

### 2.5. Ratiometric Primary Self-Referencing Thermometric Properties

To assess the potential application of PHTF-3Eu as ratiometric primary self-referencing thermometer, we adopted a recently proposed approach based on the analysis of the photoluminescence excitation (PLE) spectra of  $\text{Eu}^{3+}$  [40]. As shown in Figure 6a, the broad ligand and the narrow  $\text{Eu}^{3+}$  PLE bands monitored at 612 nm, corresponding to the most intense  $\text{Eu}^{3+} {}^5\text{D}_0 \rightarrow {}^7\text{F}_2$  emission line, display a strong dependence from temperature. For metal-centered excitation, this is related to the close J energy levels structure of the ground level manifold  ${}^7\text{F}_J$ , with  $J = 0, 1 \dots 6$ , where the first three levels, lying within  $\sim 1000 \text{ cm}^{-1}$  energy separation, are thermally coupled even below 400 K. As the temperature increases, the  ${}^7\text{F}_0$  level population is depleted in favor of the population of the  ${}^7\text{F}_{1,2}$  levels following a Boltzmann distribution. Under the legit assumption that the integrated intensities of the related excitation bands are proportional to the number of emitters of a certain  ${}^5\text{D}_J$  state fed by a specific  ${}^7\text{F}_J$  level ( $J = 0, 1, 2$ ), a known thermometric equation can be written:

$$\Delta_i = A_i e^{-\Delta E_i/k_B T} = \frac{I_{J'}}{I_J} \quad (4)$$

where the thermometric parameter  $\Delta_i$  refers to the ratio of the integrated intensities ( $I_{J'}$ ) of the  $i$ -th transitions starting from the  ${}^7\text{F}_{J'}$  and  ${}^7\text{F}_J$  ( $J' > J$ ) levels of the low energy manifold, and  $A_i$  is a pre-exponential factor depending on the absorption transition rates, the level degeneracy, and the refractive index of the medium.  $\Delta E_i$  is the energy difference between the  ${}^7\text{F}_{J'}$  and  ${}^7\text{F}_J$  ( $J' > J$ ) levels, which can be easily retrieved from the barycenter of the excitation bands or by experimental data fitting according to Equation (4). The major advantage of using PLE instead of PL is that the temperature dependence of the optical features can be described by a known equation (Equation (4)) with easily retrievable constants, allowing for primary thermometers with internal calibration (self-referencing) of universal application. In fact, the single determination of the thermometric parameter  $\Delta_{i0}$  at a  $T_0$  temperature univocally defines Equation (4). In addition, PLE spectra are usually not affected by crystal field splitting, hence overcoming band broadening due to a distribution of emitters in different environments (as in doped inorganic, hybrid, and polymeric materials) and require low energy excitation sources thus preventing sample heating (affecting the system response to temperature changes). Therefore, the proposed

approach is fully suitable to be applied for the material under investigation. To study the ratiometric thermometric properties of PHTF-3Eu, we took primarily into consideration the bands associated to the  ${}^7F_0 \rightarrow {}^5D_1$  (525 nm) and  ${}^7F_1 \rightarrow {}^5D_1$  (535 nm) transitions since they do not overlap with other bands and are intense enough to be quantifiable. As additional reference, we also considered the  ${}^7F_0 \rightarrow {}^5D_2$  associated band (463 nm), since its relatively high intensity allows the subtraction of the contribution of the overlapping tail of the broad ligand-centered band without relevant error. As expected (Figure 6a), the intensity of the bands related to the  ${}^7F_0$  starting level decreases whereas that related to the  ${}^7F_1$  level increases with some deviations at temperatures above 370 K likely due to the increasingly sizeable thermal coupling of the  ${}^7F_2$  and  ${}^7F_3$  levels.

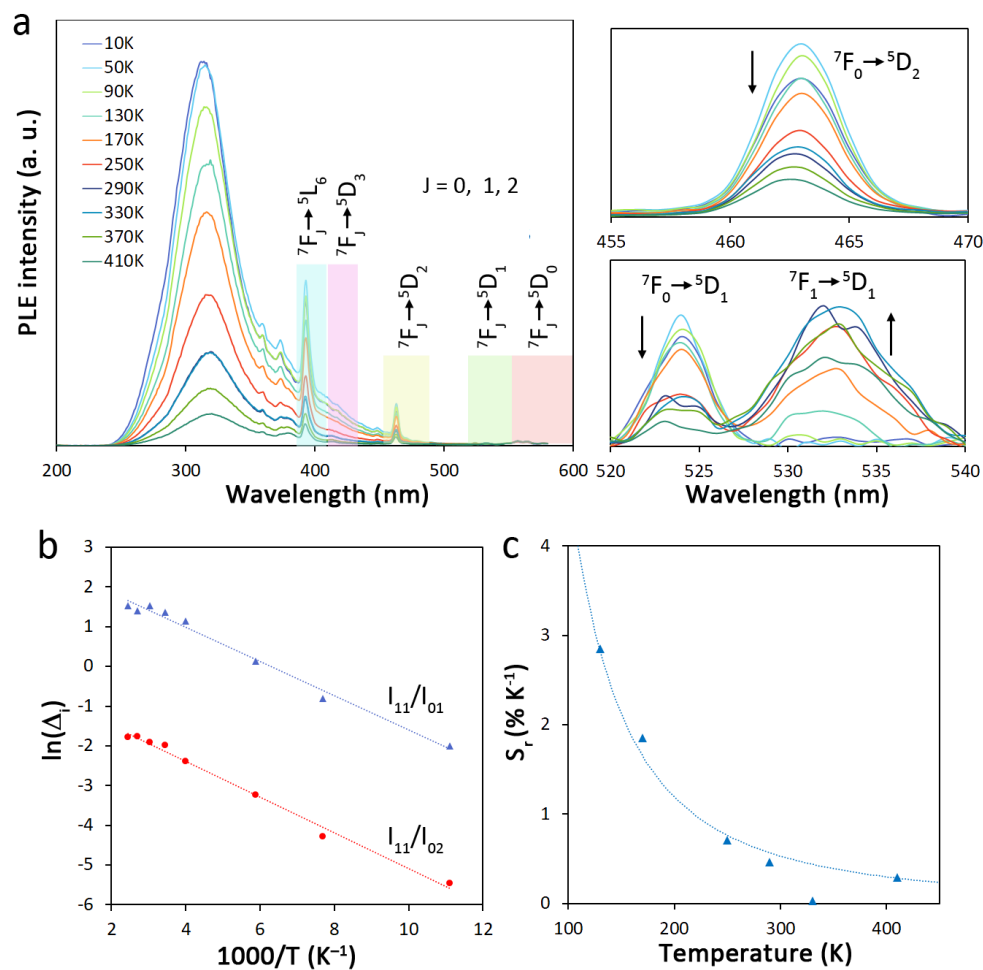


**Figure 6.** (a) Temperature-dependent PLE spectra of PHTF-3Eu monitored at 612 nm. The two insets on the right show a magnification of the bands considered for the assessment of the thermometric properties. The spectra associated to the  ${}^7F_0 \rightarrow {}^5D_2$  transition have been corrected for the overlapping contribution of the broad ligand-centered band; (b) Dependence of the natural logarithm of the thermometric parameter  $\ln\Delta_i$  from the inverse of the absolute temperature  $T$ . The dotted lines represent the best linear regression fit based on Equation (5) ( $R^2 = 0.987$  and  $0.991$  for the blue and red line, respectively); (c) Experimental  $S_r$  % values at different temperatures (blue triangles). The dotted curve represents the best fit to data according to Equation (7) (retrieved  $\Delta E = 331 \text{ cm}^{-1}$ ,  $R^2 = 0.949$ ).

Two thermometric parameters were calculated as the ratio between the integrated intensities of the band related to the  ${}^7F_1 \rightarrow {}^5D_1$  transition ( $I_{11}$ ) to the integrated intensity

of the  ${}^7F_0 \rightarrow {}^5D_1$  ( $I_{01}$ ) and  ${}^7F_0 \rightarrow {}^5D_2$  ( $I_{02}$ ) transitions and the retrieved experimental data were then fitted with Equation (4) in the linear form:

$$\ln \Delta_i = \ln A_i - \frac{\Delta E_i}{k_B} \frac{1}{T} \quad (5)$$

As shown in Figure 6b, curve fitting returns two nearly parallel lines with  $\Delta E_{01} = 300 \text{ cm}^{-1}$  and  $313 \text{ cm}^{-1}$  for  $\Delta_{01} = I_{11}/I_{01}$  and  $I_{11}/I_{02}$ , respectively, which are very close to the value retrieved from the PLE spectrum ( $322 \text{ cm}^{-1}$ ) and to the value calculated for the free ion ( $379 \text{ cm}^{-1}$ ) [25]. To further assess the potential of PHTF-3Eu as primary thermometer with self-referencing attributes, we also calculated  $\Delta_{00}$  ( $=I_{02}/I_{01}$ ) taking into account transitions from the same initial level, where  $\Delta E_i = 0$  and Equation (4) reduces to  $\Delta_i = A_i$ . Results shown in Figure S11 demonstrate the independence of this thermometric parameter from temperature, which univocally defines  $A_i$  and represents an extremely useful internal calibration to discriminate spurious effects from different matrixes/environments of the thermometer.

Another relevant parameter in luminescence thermometry is the relative sensitivity  $S_{r,i}$ , which expresses the variation of the thermometric parameter  $\Delta_i$  with temperature, and is usually defined as:

$$S_{r,i} = \frac{1}{\Delta_i} \left| \frac{d\Delta_i}{dT} \right|, \quad (6)$$

which, after differentiation, can be written as:

$$S_{r,i} = \frac{\Delta E_i}{k_B} \frac{1}{T^2}, \quad (7)$$

The experimental  $S_r$  values for the thermometric parameter calculated from the  $I_{11}/I_{01}$  ratio on dependence of the temperature are reported in Figure 6b, whereas Figure S12 reports data for the  $I_{11}/I_{02}$  thermometric parameter. Differently from PL-based thermometers, PLE-based ones yield a monotonic decrease in  $S_r$  instead of a usually observed maximum, which results from the absence of any (temperature-dependent) offset in the thermometric Equation (4) ( $\Delta = Ae^{-\Delta E/kT} + B$ ) [41]. Therefore, the experimental  $S_r$  values could be well fitted with the known Equation (7) (dotted lines in Figures 6b and S10) which is demonstrated to yield reliable general predictions of  $S_r$  at different temperatures independently from the measurement conditions (matrix/environment). This is also further confirmed by the linear trend of experimental  $S_r$  values with the inverse temperature squared  $1/T^2$  reported in Figure S13. Based on all these considerations, we can conclude that PHTF-3Eu can be successfully employed as a ratiometric self-referencing primary thermometer, particularly in the cryogenic temperature range (100–200K).

### 3. Materials and Methods

#### 3.1. Materials and Measurements

All chemicals were purchased from Sigma-Aldrich (St. Louis, MO, USA), Fisher Scientific (Waltham, MA, USA), or Sinopharm (Beijing, China) and used as received without further purification. Powder X-ray diffraction patterns were measured on a Thermo Scientific ARL X'TRA or Bruker D8 diffractometer at room temperature. Diffuse reflectance infrared Fourier transform spectroscopy (DRIFTS) measurements were recorded on a Thermo Nicolet 6700 spectrometer, equipped with a nitrogen-cooled MCTA detector and a KBr beam splitter at room temperature. Scanning electron microscopy micrographs were obtained on a SEM apparatus, type S-3000N (Hitachi). Transmission electron microscopy (TEM) was carried out by using a Cs-corrected JEOL JEM2200FS transmission electron microscope operated at 200 kV. Thermo-gravimetric analysis (TGA) and the derivative thermogravimetry (DTG) was carried out on a Netsch STA 449E3 Jupiter analyzer. Fourier transform Raman spectroscopy (FT-Raman) measurements were recorded on a Thermo Nicolet 6700 NXR FT-Raman spectrometer with an InGaAs detector at room temperature.

The CHN elemental analyses were carried out using a thermo organic elemental analysis flash 2000 apparatus. The samples' photographs were acquired using a Canon IXUS digital camera or iPhone 6s Plus mobile. The samples were placed under a Cole-Parmer laboratory UV lamp (254 or 302 or 365 nm) or irradiated by a Xe900 lamp. For the analysis of the  $\text{Ln}^{3+}$  concentrations, inductively coupled plasma mass spectrometry (ICP-MS) was carried out with a Nexion 350 spectrometer (Perkin Elmer, Akron, OH, USA). Steady state and transient photoluminescence (PL) at room temperature were performed by using an Edinburgh FLSP920 spectrophotometer equipped with a Hamamatsu R928P PMT detector. The steady state PL spectra were acquired with a 450W xenon lamp. The transient PL experiments were performed using a microsecond flashlamp (repetition rate 0.1–100 Hz) or a pulsed nanosecond EPLED laser (wavelength 331 nm). The temperature dependent measurements were performed using an ARS CS202-DMX-1SS closed cycle cryostat at low temperature range. Temperature dependent steady-state PL and PLE data were analyzed (peak integration, baseline subtraction, curve fitting) using Origin Pro 8.5 software. Spectral data were reported with reference to wavenumbers ( $\text{cm}^{-1}$ ) prior to any analysis.

### 3.2. Synthesis of PHTF and PHTF:Eu Hydrogen Bonded Heptazine Framework

A total of 3.03 g (50 mmol) of urea was dissolved in 50 mL of deionized water under stirring at 95 °C. 1.67 mL (0.1 mol/L) of  $\text{Eu}(\text{NO}_3)_3$  solution was added to the hot urea solution. Subsequently, the mixtures were magnetically stirred at 90 °C. Then, the products were dried at 95 °C for 12 h. The sample was crushed in a mortar to get a fine white precursor and labeled as U-1Eu. Then, U-1Eu was heated at a rate of 10 K/min within a muffle furnace to 255 °C under air, and kept for 90 min. The samples were cooled down passively within the furnace. In order to remove the possible residuals of unreacted urea, the obtained raw sample was further washed with deionized water and centrifuged several times. The product was additionally annealed at the same temperature (255 °C) for another 20 min under air. After the sample had been cooled down passively within the furnace, it was crushed. The final product was labelled as PHTF-1Eu. Samples with different molar ratios of urea/ $\text{Eu}^{3+}$  in 1:0, 200:1, 100:1 and 50:1 ratios were also synthesized. The samples were labelled as PHTF, PHTF-2Eu, PHTF-3Eu, and PHTF-4Eu, respectively.

## 4. Conclusions

In summary, trivalent europium ions incorporated polymeric hydrogen-bonded triazine composites have been developed. These materials can be synthesized via a facile and low-cost solid phase thermal pyrolysis route. Under excitation with UV light, the materials emit bright red luminescence of high colour purity. The PL quantum yield for PHTF-3Eu is 19.2%, much higher than the value obtained for the urea-based precursor U-3Eu (5.5%), due to the high sensitization efficiency (41.8%) and intrinsic quantum yield (45.9%) in the dehydrated system. The PHTF:Eu samples can keep stable colour purity in the temperature range from 10 K to 410 K. The activation energy of PHTF-3Eu, retrieved through temperature-dependent PL measurements, is found to be ~89 meV, which is a value much higher than many popular inorganic and organic emitters, indicating a high stability of the emission intensity upon temperature increase. A thermal deactivation mechanism through crossover via energy back transfer to the ligand triplet state or to a low-lying ligand-to-metal CT state is proposed to account for the emission intensity dependence on temperature. The luminescence thermometric properties of PHTF:Eu have been investigated by adopting a novel approach based on the use of excitation spectra, which yielded a fully univocally determined thermometric equation of general validity. It has been demonstrated that the presented  $\text{Eu}^{3+}$  doped hydrogen bonded triazine frameworks can be successfully employed as ratiometric primary self-referencing thermometers with excellent sensitivity in the cryogenic temperature range.

**Supplementary Materials:** The following supporting information can be downloaded at: <https://www.mdpi.com/article/10.3390/molecules27196687/s1>, Table S1: CHN analysis, Figure S1. PXRD patterns, Table S2: ICP-MS analysis, Figure S2: SEM images and STEM-EDX elemental mapping, Figure S3: DLS data, Figure S4: FT-Raman spectra, Figure S5: Additional room temperature PL data, Table S3: Assignment of  $\text{Eu}^{3+}$  peaks, Table S4: CIE chromaticity coordinates at room temperature, Table S5: Fitting results of the decay curves, Photophysical Parameters discussion, Figure S6: Quantum yield determination spectra, Figure S7: PL decay curves of U-3Eu, Table S6: fitting results of the decay curve of U-3Eu, Figure S8: Energy levels diagrams, Figure S9. Normalized emission spectra at different temperatures, Figure S10. Additional data and fittings for the thermal dependence of the integrated PL intensity, Table S7: Fitting parameters for the thermometric equation, Table S8: CIE coordinates at different temperatures, Figure S11: Dependence of  $\Delta_{02/01}$  from the temperature, Figure S12:  $S_r\%$  for  $\Delta_{01} = I_{11}/I_{02}$ , Figure S13: Linear trend of experimental  $S_r\%$  values with  $1/T^2$ .

**Author Contributions:** Conceptualization, C.Y., F.A. and R.V.D.; Data curation, C.Y. and D.M.; Formal analysis, F.A.; Funding acquisition, R.V.D.; Investigation, C.Y., D.M. and J.G.; Methodology, C.Y., D.M. and F.A.; Supervision, F.A. and R.V.D.; Writing—original draft, C.Y. and F.A.; Writing—review & editing, C.Y., D.M., J.G., F.A. and R.V.D. All authors have read and agreed to the published version of the manuscript.

**Funding:** This research was funded by Office of Naval Research Global grant number N62902-22-1-2024.

**Institutional Review Board Statement:** Not applicable.

**Informed Consent Statement:** Not applicable.

**Data Availability Statement:** The data presented in this study are available on request from the corresponding author.

**Acknowledgments:** We thank Funda Aliç (UGent) for CHN elemental analyses. D.M acknowledges the support of the Office of Naval Research Global through the Research Grant N62902-22-1-2024.

**Conflicts of Interest:** The authors declare no conflict of interest.

**Sample Availability:** Samples of the compounds PHTF and PHTF:Eu cited in this work are available from the authors upon reasonable request.

## References

1. Lin, R.-B.; He, Y.; Li, P.; Wang, H.; Zhou, W.; Chen, B. Multifunctional porous hydrogen-bonded organic framework materials. *Chem. Soc. Rev.* **2019**, *48*, 1362. [CrossRef] [PubMed]
2. Beatty, A.M. Open-framework coordination complexes from hydrogen-bonded networks: Toward host/guest complexes. *Coord. Chem. Rev.* **2003**, *246*, 131. [CrossRef]
3. Asatkar, A.K.; Bedi, A.; Zade, S.S. Metallo-organic conjugated systems for organic electronics. *Isr. J. Chem.* **2014**, *54*, 467. [CrossRef]
4. Asatkar, A.K.; Senanayak, S.S.; Bedi, A.; Panda, S.; Narayan, K.S.; Zade, S.S. Zn(II) and Cu(II) complexes of a new thiophene-based salphen-type ligand: Solution-processable high-performance field-effect transistor materials. *Chem. Commun.* **2014**, *50*, 7036. [CrossRef] [PubMed]
5. Vallan, L.; Urriolabeitia, E.P.; Ruipérez, F.; Matxain, J.M.; Canton-Vitoria, R.; Tagmatarchis, N.; Benito, A.M.; Maser, W.K. Supramolecular-enhanced charge-transfer within entangled polyamide chains as origin of the universal blue fluorescence of polymer carbon dots. *J. Am. Chem. Soc.* **2018**, *140*, 12862. [CrossRef] [PubMed]
6. Brites, C.D.S.; Millán, A.; Carlos, L.D. Lanthanides in Luminescent Thermometry. In *Handbook on the Physics and Chemistry of Rare Earths*; Elsevier: Amsterdam, The Netherlands, 2016; Volume 49, Chapter 281.
7. Yang, C.; Liu, J.; Ma, L.; Li, A.; Liu, Z. Synthesis and structure change of graphene oxide/GdF<sub>3</sub>: Yb, Er nanocomposites with improved upconversion luminescence. *Mater. Res. Bull.* **2016**, *84*, 283. [CrossRef]
8. Melby, L.; Rose, N.; Abramson, E.; Caris, J. Synthesis and Fluorescence of Some Trivalent Lanthanide Complexes. *J. Am. Chem. Soc.* **1964**, *86*, 5117. [CrossRef]
9. Carnall, W.T.; Fields, P.R.; Rajnak, K. Electronic Energy Levels in the Trivalent Lanthanide Aquo Ions. I. Pr<sup>3+</sup>, Nd<sup>3+</sup>, Pm<sup>3+</sup>, Sm<sup>3+</sup>, Dy<sup>3+</sup>, Ho<sup>3+</sup>, Er<sup>3+</sup>, and Tm<sup>3+</sup>. *J. Chem. Phys.* **1968**, *49*, 4424. [CrossRef]
10. Yang, C.; Folens, K.; Du Laing, G.; Artizzu, F.; Van Deun, R. Improved Quantum Yield and Excellent Luminescence Stability of Europium-Incorporated Polymeric Hydrogen-Bonded Heptazine Frameworks Due to an Efficient Hydrogen-Bonding Effect. *Adv. Funct. Mater.* **2020**, *30*, 2003656. [CrossRef]
11. Yang, C.; Kaczmarek, A.M.; Folens, K.; Du Laing, G.; Vrielinck, H.; Khelifi, S.; Li, K.; Van Deun, R. Lanthanide-centered luminescence evolution and potential anti-counterfeiting application of Tb<sup>3+</sup>/Eu<sup>3+</sup> grafted melamine cyanurate hydrogen-bonded triazine frameworks. *Mater. Chem. Front.* **2019**, *3*, 579. [CrossRef]

12. Yang, C.; Zhao, W.; Yu, X.; Liu, H.; Liu, J.; Van Deun, R.; Liu, Z. Facile synthesis and luminescence property of core-shell structured NaYF<sub>4</sub>: Yb, Er/g-C<sub>3</sub>N<sub>4</sub> nanocomposites. *Mater. Res. Bull.* **2017**, *94*, 415. [CrossRef]
13. Yang, C.; Artizzu, F.; Folens, K.; Du Laing, G.; Van Deun, R. Excitation dependent multicolour luminescence and colour blue-shifted afterglow at room-temperature of europium incorporated hydrogen-bonded multicomponent frameworks. *J. Mater. Chem. C* **2021**, *9*, 7154. [CrossRef]
14. Feng, J.; Yan, X.; Liu, T.; Cao, R. Fabrication of Lanthanide-Functionalized Hydrogen-Bonded Organic Framework Films for Ratiometric Temperature Sensing by Electrophoretic Deposition. *ACS Appl. Mater. Interfaces* **2020**, *12*, 29854. [CrossRef] [PubMed]
15. He, L.; Liu, Y.; Lin, M.; Awika, J.; Ledoux, D.R.; Li, H.; Mustapha, A. A new approach to measure melamine, cyanuric acid, and melamine cyanurate using surface enhanced Raman spectroscopy coupled with gold nanosubstrates. *Sens. Instrum. Food Qual.* **2008**, *2*, 66. [CrossRef]
16. Pérez-Manríquez, L.; Cabrera, A.; Sansores, L.E.; Salcedo, R. Aromaticity in cyanuric acid. *J. Mol. Mod.* **2011**, *17*, 1311. [CrossRef]
17. Schaber, P.M.; Colson, J.; Higgins, S.; Thielen, D.; Anspach, B.; Brauer, J. Thermal decomposition (pyrolysis) of urea in an open reaction vessel. *Thermochim. Acta* **2004**, *424*, 131. [CrossRef]
18. Koglin, E.; Kip, B.J.; Meier, R.J. Adsorption and Displacement of Melamine at the Ag/Electrolyte Interface Probed by Surface-Enhanced Raman Microprobe Spectroscopy. *J. Phys. Chem.* **1996**, *100*, 5078. [CrossRef]
19. Papailias, I.; Giannakopoulou, T.; Todorova, N.; Demotikali, D.; Vaimakis, T.; Trapalis, C. Effect of processing temperature on structure and photocatalytic properties of g-C<sub>3</sub>N<sub>4</sub>. *App. Surf. Sci.* **2015**, *358*, 278. [CrossRef]
20. Nag, A.; Schmidt, P.J.; Schnick, W. Synthesis and Characterization of Tb[N(CN)<sub>2</sub>]<sub>3</sub>·2H<sub>2</sub>O and Eu[N(CN)<sub>2</sub>]<sub>3</sub>·2H<sub>2</sub>O: Two New Luminescent Rare-Earth Dicyanamides. *Chem. Mater.* **2006**, *18*, 5738. [CrossRef]
21. International Telecommunication Union, Recommendation ITU-R BT.2020-2 Parameter Values for Ultra-High Definition Television Systems for Production and International Programme Exchange 10/2015. Available online: [https://www.itu.int/dms\\_pubrec/itu-r/rec/bt/R-REC-BT.2020-2-201510-I!!PDF-E.pdf](https://www.itu.int/dms_pubrec/itu-r/rec/bt/R-REC-BT.2020-2-201510-I!!PDF-E.pdf) (accessed on 7 September 2022)
22. Aebischer, A.; Gumy, F.; Bünzli, J.-C.G. Intrinsic quantum yields and radiative lifetimes of lanthanide tris(dipicolinates). *Phys. Chem. Chem. Phys.* **2009**, *11*, 1346. [CrossRef]
23. Mara, D.; Artizzu, F.; Smet, P.F.; Kaczmarek, A.M.; Van Hecke, K.; Van Deun, R. Vibrational Quenching in Near-Infrared Emitting Lanthanide Complexes: A Quantitative Experimental Study and Novel Insights. *Chem. Eur. J.* **2019**, *25*, 15944. [CrossRef] [PubMed]
24. Heine, J.; Müller-Buschbaum, K. Engineering metal-based luminescence in coordination polymers and metal-organic frameworks. *Chem. Soc. Rev.* **2013**, *42*, 9232. [CrossRef] [PubMed]
25. Binnemans, K. Interpretation of europium(III) spectra. *Coord. Chem. Rev.* **2015**, *295*, 1. [CrossRef]
26. Werts, M.H.; Jukes, R.T.; Verhoeven, J.W. The emission spectrum and the radiative lifetime of Eu<sup>3+</sup> in luminescent lanthanide complexes. *Phys. Chem. Chem. Phys.* **2002**, *4*, 1542. [CrossRef]
27. Chen, J.; Meng, Q.; May, P.S.; Berry, M.T.; Lin, C. Dipicolinate Sensitization of Europium Luminescence in Dispersible 5%Eu:LaF<sub>3</sub> Nanoparticles. *J. Phys. Chem. C* **2013**, *117*, 5953. [CrossRef]
28. Artizzu, F.; Loche, D.; Mara, D.; Malfatti, L.; Serpe, A.; Van Deun, R.; Casula, M.F. Lighting up Eu<sup>3+</sup> luminescence through remote sensitization in silica nanoarchitectures. *J. Mater. Chem. C* **2018**, *6*, 7479. [CrossRef]
29. Seitz, F. An interpretation of crystal luminescence. *Trans. Faraday Soc.* **1939**, *35*, 74. [CrossRef]
30. Duarte, M.; Martins, E.; Baldochi, S.L.; Vieira, N.D.; Vieira, M.M.M. De-excitation mechanisms of BaLiF<sub>3</sub>:Co<sup>2+</sup> crystals. *Opt. Commun.* **1999**, *159*, 221. [CrossRef]
31. Das, D.; Shinde, S.; Nanda, K. Temperature-Dependent Photoluminescence of g-C<sub>3</sub>N<sub>4</sub>: Implication for Temperature Sensing. *ACS App. Mater. Interfaces* **2016**, *8*, 2181. [CrossRef]
32. Yu, P.; Wen, X.; Toh, Y.-R.; Tang, J. Temperature-Dependent Fluorescence in Carbon Dots. *J. Phys. Chem. C* **2012**, *116*, 25552. [CrossRef]
33. Karczewski, G.; Maćkowski, S.; Kutrowski, M.; Wojtowicz, T.; Kossut, J. Photoluminescence study of CdTe/ZnTe self-assembled quantum dots. *App. Phys. Lett.* **1999**, *74*, 3011. [CrossRef]
34. Varshni, Y.P. Temperature dependence of the energy gap in semiconductors. *Physica* **1967**, *34*, 149. [CrossRef]
35. Hao, Z.; Yang, G.; Song, X.; Zhu, M.; Meng, X.; Zhao, S.; Song, S.; Zhang, H. A europium(III) based metal-organic framework: Bifunctional properties related to sensing and electronic conductivity. *J. Mater. Chem. A* **2014**, *2*, 237. [CrossRef]
36. Berry, M.T.; May, P.S.; Xu, H. Temperature Dependence of the Eu<sup>3+</sup><sup>5</sup>D<sub>0</sub> Lifetime in Europium Tris(2,2,6,6-tetramethyl-3,5-heptanedionato). *J. Phys. Chem.* **1996**, *100*, 9216. [CrossRef]
37. Lahoud, M.G.; Frem, R.C.G.; Gálico, D.A.; Bannach, G.; Nolasco, M.M.; Ferreira, R.A.S.; Carlos, L.D. Intriguing light-emission features of ketoprofen-based Eu(III) adduct due to a strong electron-phonon coupling. *J. Lumin.* **2016**, *170*, 357. [CrossRef]
38. Kim, M.; Jeon, S.K.; Hwang, S.-H.; Lee, J.Y. Molecular design of triazine and carbazole based host materials for blue phosphorescent organic emitting diodes. *Phys. Chem. Chem. Phys.* **2015**, *17*, 13553. [CrossRef]
39. Quochi, F.; Saba, M.; Artizzu, F.; Mercuri, M.L.; Deplano, P.; Mura, A.; Bongiovanni, G. Ultrafast dynamics of intersystem crossing and resonance energy transfer in Er(III)-quinolinolate complexes. *J. Phys. Chem. Lett.* **2010**, *1*, 2733. [CrossRef]

40. De Souza, K.M.N.; Silva, R.N.; Silva, J.A.B.; Brites, C.D.S.; Francis, B.; Ferreira, R.A.S.; Carlos, L.D.; Longo, R.L. Novel and High-Sensitive Primary and Self-Referencing Thermometers Based on the Excitation Spectra of Lanthanide Ions. *Adv. Opt. Mater.* **2022**, *10*, 2200770. [[CrossRef](#)]
41. Li, L.; Zhou, Y.; Qin, F.; Zheng, Y.; Zhao, H.; Zhang, Z. Modified calculation method of relative sensitivity for fluorescence intensity ratio thermometry. *Opt. Lett.* **2017**, *42*, 4837. [[CrossRef](#)]